

A wavelet method for metal artifact reduction with multiple metallic objects in the field of view¹

Shiying Zhao^{a,b}, Kyongtae T. Bae^c, Bruce Whiting^d and Ge Wang^e

^a*Department of Mathematics and Computer Science, University of Missouri-St. Louis, St. Louis, MO 63121, USA*

E-mail: zhao@arch.umsl.edu

^b*Mallinckrodt Institute of Radiology, Washington University, St. Louis, MO 63110, USA*

^c*E-mail: baet@mir.wustl.edu*

^d*E-mail: bwhiting@wuerl.wustl.edu*

^e*Department of Radiology, University of Iowa, Iowa City, IA 52242, USA*

E-mail: ge-wang@uiowa.edu

Abstract. Image artifacts induced by multiple metallic objects pose a persistent problem in X-ray computed tomography (CT). Among existing CT methods for metal artifact reduction, the wavelet-based approach we recently developed is very promising in practice. In this paper, we report a major refinement to our earlier work [1]. The key component of this refinement is a novel weighting scheme for wavelet multiresolution interpolation. This weighting scheme is designed specifically to take into account multiple metallic implants in the field of view. In contrast to commonly used noniterative algorithms, our algorithm identifies and corrects most seriously corrupted projection data based on wavelet multiresolution analysis. Experimental results indicate that the proposed algorithm significantly improves the image quality, and clearly reveals anatomic details in the immediate vicinity of multiple metallic implants.

Keywords: X-ray computed tomography (CT), metal artifact reduction (MAR), image quality, wavelet, multiresolution

1. Introduction

Despite recent progress in X-ray computed tomography (CT), artifacts due to metallic objects with high atomic numbers still significantly limit several important clinical applications, including orthopedic, dental and spine imaging. These artifacts severely impair visualization and quantification of anatomic and/or pathologic features, especially in the presence of multiple metallic implants in the field of view (FOV). A wavelet multiresolution interpolation (WMI) approach for metal artifact reduction (MAR) was recently proposed in [1], in which a short review of various MAR algorithms was also given. The current study is a major refinement to our previous work. The emphasis here is to handle the most difficult cases in which *multiple* metallic objects present in the FOV.

¹This work was supported in part by the Whitaker Foundation (Biomedical Engineering Program, RG-98-0448).

It is well-known from the CT physics that the amount of X-ray attenuation is proportional to the path length through an object and the attenuation coefficients of the constituent materials. When there are multiple metallic objects in the FOV, the high attenuation effects such as beam hardening and scatter result nonlinear attenuation measurements. Consequently, streak artifacts between the objects are most prominent in the reconstructed images. Recent experimental studies [2,3] revealed that the presence of multiple metallic objects within a single CT slice magnifies CT artifacts to the degree that is far greater than the sum of the effects due to each of these individual objects.

Traditional noniterative methods assume metallic implants being completely opaque to X-ray beams in the diagnostic energy range, and hence data gaps are either bridged by polynomial interpolations or filled with data satisfying consistency criteria [4–8]. As a consequence, anatomic details between and/or surrounding the implants are extremely difficult to be recovered, since most of directly relevant data are replaced artificially. On the contrary, our WMI processes corrupted projection data more intelligently, although it is also based on the traditional gap-interpolation algorithms. The main difference between the traditional methods and ours is that the traditional methods somehow replace corrupted data entirely, while our method identifies wavelet components that are most seriously damaged then effectively corrects the data in the wavelet domain.

In this paper, we introduce a new weighting scheme for WMI to keep crucial diagnostic information as much as possible while reducing artifacts induced by multiple metallic objects in the FOV. Our experiments with physical phantoms and clinical dental scans demonstrate that our method produces significantly better image quality than the most popular MAR with linear-interpolation. Finally, the merits, limitations and potentials of our algorithm are discussed.

2. Materials and methods

To describe the proposed weighting scheme, we first recall the basic setting for the WMI presented in [1]. We suppose that an image to be recovered from its X-ray scan data is a piecewise smooth function defined inside the FOV, and its support contains finitely many disjoint cross-sections of metallic objects, $\Omega_1, \dots, \Omega_n$, which are quasi-disks in the sense that there are constants $r > 0$ and $c > 1$ such that $B(x_m, r) \subset \Omega_m \subset B(x_m, cr)$, where $B(x_m, r)$ denotes the disk of radius r centered at $x_m \in \Omega_m$, $m = 1, 2, \dots, n$.

We denote $g_\beta(\alpha)$ the scan data in the equi-angular fan-beam geometry [9,10] with the source angular position β and ray angular position α . In practice, the metallic set $\Omega^M = \bigcup_{m=1}^n \Omega_m$ can be estimated by taking one or more proper threshold levels in the image reconstructed from the scan data g , and the projection, g_β^M , of Ω^M is then approximated from the numerical reprojection, $\text{rp}_\beta(\Omega^M)$, of Ω^M .

Let g_β^{L+M} be the estimated g_β via linear interpolation. More precisely, by expressing Ω_β^M , the “shadow” of Ω^M with the source angular position β , as a union of non-empty disjoint intervals $\{(p_i, q_i) : i \in I_\beta\}$, $g_\beta^{L+M}(\alpha)$ is defined as $g_\beta(\alpha)$ if $\alpha \notin \Omega_\beta^M$, and

$$g_\beta^{L+M}(\alpha) = \frac{q_i - \alpha}{q_i - p_i} g_\beta(p_i) + \frac{\alpha - p_i}{q_i - p_i} g_\beta(q_i) + g_\beta^M(\alpha) \quad (1)$$

if $\alpha \in (p_i, q_i)$ for some index $i \in I_\beta$.

Let $\{\psi, \tilde{\psi}\}$ be a pair of compactly supported biorthogonal wavelets with scaling functions $\{\phi, \tilde{\phi}\}$ [11, 12]. As usual, we denote $\psi_{j,k}(\alpha) = 2^{j/2} \psi(2^j \alpha - k)$.

For each fixed β , let $\tilde{c}_{\ell,k}$ and $\tilde{d}_{j,k}$ ($\ell, j, k \in \mathbf{Z}$) denote the scaling and wavelet coefficients of the scan data g_β , and $\tilde{c}_{\ell,k}^{L+M}$ and $\tilde{d}_{j,k}^{L+M}$ the counterparts for g_β^{L+M} . The objective of WMI is to design a weighting scheme for selecting the weights $0 \leq \lambda_{j,k} \leq 1$ so that the synthesized data

$$g_\beta^R(\alpha) = \sum_{k \in \mathbf{Z}} \tilde{c}_{\ell,k}^{L+M} \phi_{\ell,k}(\alpha) + \sum_{j \geq \ell} \sum_{k \in \mathbf{Z}} \tilde{d}_{j,k}^R \psi_{j,k}(\alpha) \quad (2)$$

from the modified wavelet coefficients:

$$\tilde{d}_{j,k}^R = \lambda_{j,k} \tilde{d}_{j,k} + (1 - \lambda_{j,k}) \tilde{d}_{j,k}^{L+M}, \quad j \geq \ell, k \in \mathbf{Z}, \quad (3)$$

can suppress streak-like disturbance and recover critical information hidden in the scan data g_β . Two basic weighting schema for WMI were proposed in [1].

In this paper, we present a new weighting procedure, *multicell weighting scheme*, designed specifically for the cases of multiple metallic objects in the FOV. For each metallic cross-section Ω_m , we first compute the reprojections $\text{rp}_\beta(\Omega_m)$ for all source angular positions β , and their wavelet coefficients $\{\text{rp}_{\beta,j}(\Omega_m)(k) : k \in \mathbf{Z}\}$ at the scale-level j . For a fixed j , we define the subset S_j^M of the metal trace $\text{spt}(\text{rp}_{\beta,j}(\Omega^M))$ in the wavelet domain by

$$S_j^M = \bigcup_{\substack{l,m=1 \\ l \neq m}}^n \text{spt}(\text{rp}_{\beta,j}(\Omega_l)) \cap \text{spt}(\text{rp}_{\beta,j}(\Omega_m)), \quad (4)$$

where $\text{spt}(\text{rp}_{\beta,j}(\Omega_m))$ denotes the support of $\text{rp}_{\beta,j}(\Omega_m)$. Let $\chi_{S_j^M}$ be the indicator function of the set S_j^M , we then define the weights $\lambda_{j,k}$ as $0 \leq s_j \leq 1$ multiplying the N -fold discrete convolution of the function $1 - \chi_{S_j^M}$ for some positive integer N , that is,

$$\lambda_{j,k} = s_j \underbrace{(1 - \chi_{S_j^M}) * \cdots * (1 - \chi_{S_j^M})}_{N \text{ times}}(k). \quad (5)$$

The rationale behind the multicell weighting scheme is based on the multiresolution analysis for MAR given in [1]. First of all, by definition Eq. (4), the sets S_j^M can be identified as the source of massive streak artifacts emanating from the objects. Points in S_j^M relate to those X-rays that are associated with longer paths through metallic objects (passing at least two objects) during a CT scan. Secondly, weights $\lambda_{j,k}$ defined by Eq. (5) take values close to zero around the center line of S_j^M at each scale-level j . If these weights are used, severe truncation of scan data g_β due to the effect of attenuation will be mostly diminished. Thirdly, the self-convolution of the function $1 - \chi_{S_j^M}$ yields a smoother function that takes values close to 1 near the boundaries of S_j^M . As we analyzed in [1], for scale-level j at which the size of $\text{spt}(\tilde{\psi}_{j,0})$ is comparable with the size or width of S_j^M , $\tilde{d}_{j,k}$ becomes more reliable than $\tilde{d}_{j,k}^{L+M}$ when the support of $\tilde{\psi}_{j,k}$ moves closer to the boundary of S_j^M from its interior. Therefore, by choosing the multiplier s_j equal or close to 1, it allows the less contaminated wavelet components contribute more to image reconstruction, and helps to reveal information between and/or surrounding the metallic objects. Finally, for a coarse scale-level j , we can make s_j equal or close to 0 in favor of $\tilde{d}_{j,k}^{L+M}$ to reduce the low frequency bright and dark ‘‘starburst’’ artifacts, and we should do the same at finer scale-levels if noise is strong near the boundaries.

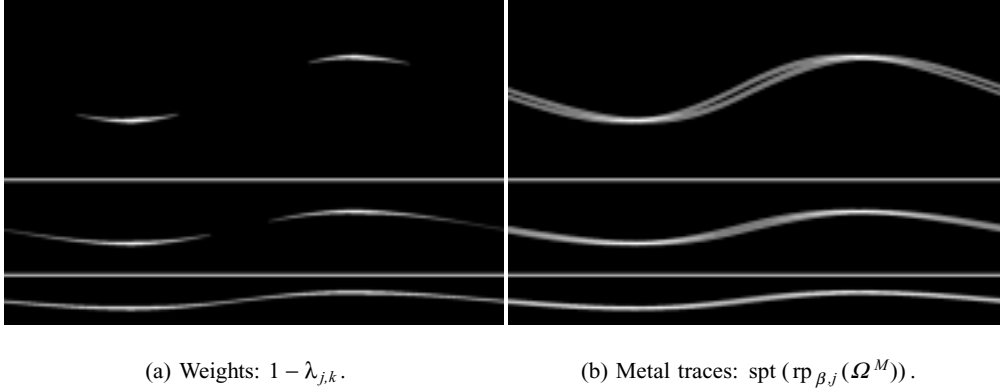


Fig. 1. Example of three-level ($j = 6, 5, 4$ from top to bottom) multicell weighting for WMI.

As an example, Fig. 1 illustrates three-level multicell weighting in the wavelet domain. Figure 1(a) displays the weights $1 - \lambda_{j,k}$ for scale-levels $j = 6, 5, 4$ (from top to bottom) in an experiment of a phantom of two copper cylinders (for detail, see the next section). The metal traces of the two copper cylinders, $\text{spt}(rp_{\beta,j}(\Omega^M))$, in the wavelet domain are shown in Fig. 1(b). The bright regions are where the scan data are considered mostly damaged, and $\tilde{d}_{j,k}^{L+M}$ are used to replace the wavelet coefficients $\tilde{d}_{j,k}$. The grey regions are where $\tilde{d}_{j,k}$ are less damaged, and the original wavelet coefficients $\tilde{d}_{j,k}$ are dominating in the interpolation Eq. (3).

We remark that it is often found useful to apply interpolation Eq. (3) directly in the projection domain, that is

$$g_{\beta}^B(\alpha) = \lambda_{\beta,\alpha} g_{\beta}(\alpha) + (1 - \lambda_{\beta,\alpha}) g_{\beta}^{L+M}(\alpha). \quad (6)$$

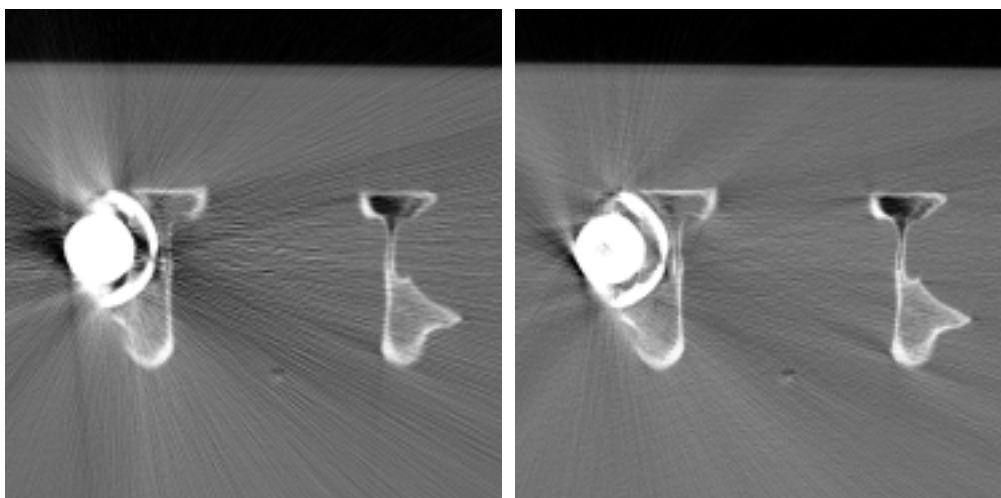
In our current work, we use the following modification of the boundary weighting scheme proposed in [1] for WMI in the projection domain. For a given boundary interpolation length L and each $i \in I_{\beta}$ (see Eq. (1) above), we let $L_i = \min\left(\frac{q_i - p_i}{2}, L\right)$, and define the weights

$$\lambda_{\beta,\alpha} = \begin{cases} 1 - b\left(\frac{\alpha - p_i}{L_i}\right); & \text{if } p_i \leq \alpha \leq p_i + L_i \\ 1 - b\left(\frac{q_i - \alpha}{L_i}\right); & \text{if } q_i - L_i \leq \alpha \leq q_i \\ 0; & \text{if } p_i + L_i < \alpha < q_i - L_i \end{cases} \quad (7)$$

where $b(t)$ is a smooth crossing function defined on the unit interval $[0, 1]$ which takes value 0 at $t = 0$ and 1 at $t = 1$:

$$b(t) = 6t^5 - 15t^4 + 10t^3. \quad (8)$$

For comparison, we also use a modified multicell weighting Eq. (5) in the projection domain to illustrate the advantages and shortcomings of the multiresolution weighting scheme.



(a) CT image of an adult pelvis with a metallic femoral head inserted.

(b) CT image with boundary weighting in the projection domain.

Fig. 2. Phantom experiment I.

3. Results

To evaluate the performance of the proposed methods discussed in the preceding section, two physical phantoms and two clinical dental CT scans were experimented. Note that these two phantom scans were previously used in [1] for testing WMI with boundary weighting.

The first physical phantom was used to test the boundary weighting procedure, Eq. (7), in the projection domain. In this experiment, a metal-backed acetabular prosthesis (Osteonics, Allendale, NJ) was fit into the left acetabulum of an adult cadaver pelvis, then a metallic femoral head was inserted into the acetabular prosthesis. The phantom was placed into a specially designed holder in a water bath and CT-scanned using a Siemens Somatom Plus S scanner (Siemens Medical Systems, Erlangen, Germany). The full-scan data set contains 1242 views and 1520 channels per view.

Figure 2(b) shows the image reconstructed by applying interpolation Eq. (6) with boundary weighting Eq. (7) in the projection domain, with the boundary interpolation length $L = 150\Delta\alpha$, where $\Delta\alpha$ is the length of scanning sample interval for the ray angle α . The image is excellent in terms of the clear bony structure and substantially reduced artifacts. Comparing with WMI [1], boundary weighting in the projection domain is more straightforward, and usually produces similar or sometimes better image quality for a single metallic object with high-resolution scans. Decreasing the length of boundary interpolation could reduce the remaining artifacts, as well as some details of features of interests.

The second phantom experiment was designed to create metal artifacts during CT scans with two metal objects in the FOV. Three polyvinyl chloride (PVC) plumbing tubes with outer diameter 2.13 cm and inner diameter 1.52 cm were placed in a water bath to simulate bone structures, with density 2300 in Hounsfield units (HU). After placing two copper cylinders with diameters 0.635 cm and 0.952 cm between the PVC tubes, CT scan data were acquired on a Siemens Somatom Plus 4 scanner (Siemens Medical Systems, Erlangen, Germany) with 120 kVp and 200 mA, via sequential (non-helical) acquisition with 768 channels per view and 1056 views.

Finally, two dental CT scans were selected from clinical cases, for which the scan settings are the same as the one for the second phantom.

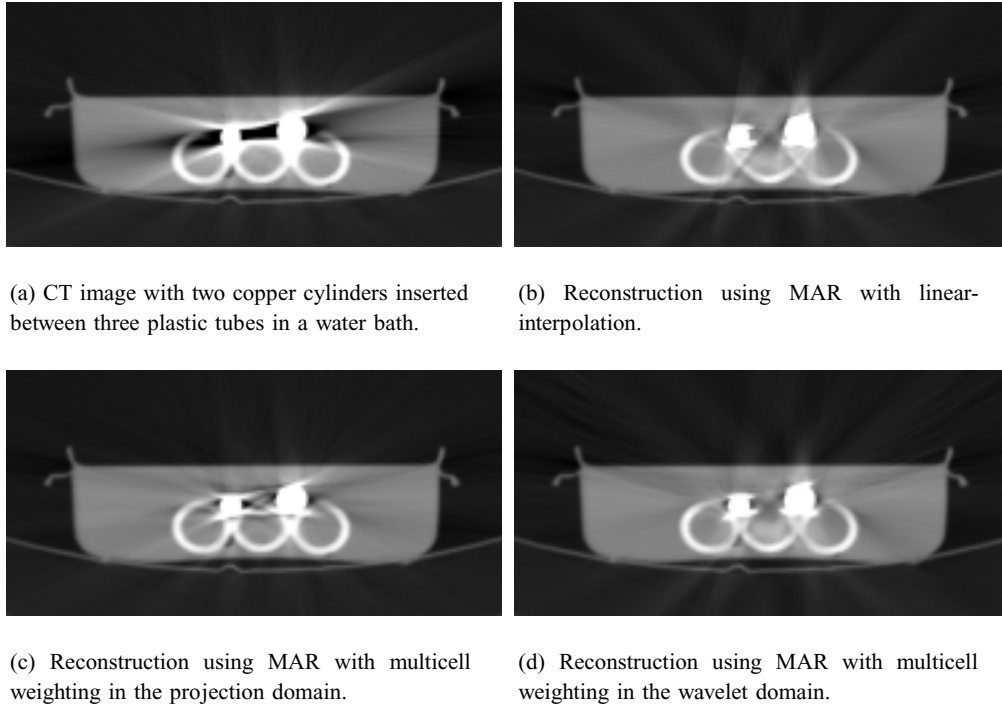


Fig. 3. Phantom experiment II.

In these tests, four sets of images were generated from 1) filtered-backprojection, 2) MAR with linear-interpolation, 3) MAR with multicell weighting in the projection domain, and 4) MAR with WMI in the wavelet domain.

For WMI, the biorthogonal spline wavelet with parameters (3, 5) [11] was used, the convolution multiplicity N was set to 3, and the multipliers s_j was set to 1 for the highest three scale-levels and 0 for rest of coarser scale-levels. The weights used in the second phantom experiment is shown in Fig. 1(a). The intersection of metal traces of the two copper cylinders is shown in Fig. 1(b). In the two cases of clinical dental scans, massive metal fillings were grouped as three metallic objects, one on the left and two on the right in both of the cases. The intersection of metal traces of the metal fillings from the same side was excluded from the sets S_j^M (right side in both cases), since the metal artifacts between these objects are not substantial. Moreover, the boundary weighting in the projection domain was also incorporated in WMI, with boundary interpolation lengths $L = 4\Delta\alpha$ and $10\Delta\alpha$, respectively. These modifications allowed us to extract more details in the vicinity of the metal fillings, especially between fillings on the right side.

As shown in Figs 3, 4 and 5, image quality comparison is consistent for each method in all the tests. Conventional CT reconstruction produced massive bright and dark streaks between the metallic objects. MAR with linear-interpolation eliminated almost all startburst artifacts, but failed to show details in the vicinity of Ω^M , especially in the region between the metallic objects. In the worst case, Fig. 5(b), the two teeth between metal fillings disappeared completely. Interpolation with multicell weighting in the projection domain, on the other hand, allowed to show rich details of the surrounding region, but failed to effectively reduce the artifacts. WMI with multicell weighting was successful to meet requirements in both of the aspects, that is, it eliminated most of artifacts while features of interest were truthfully displayed, even in the vicinity between the metallic objects.

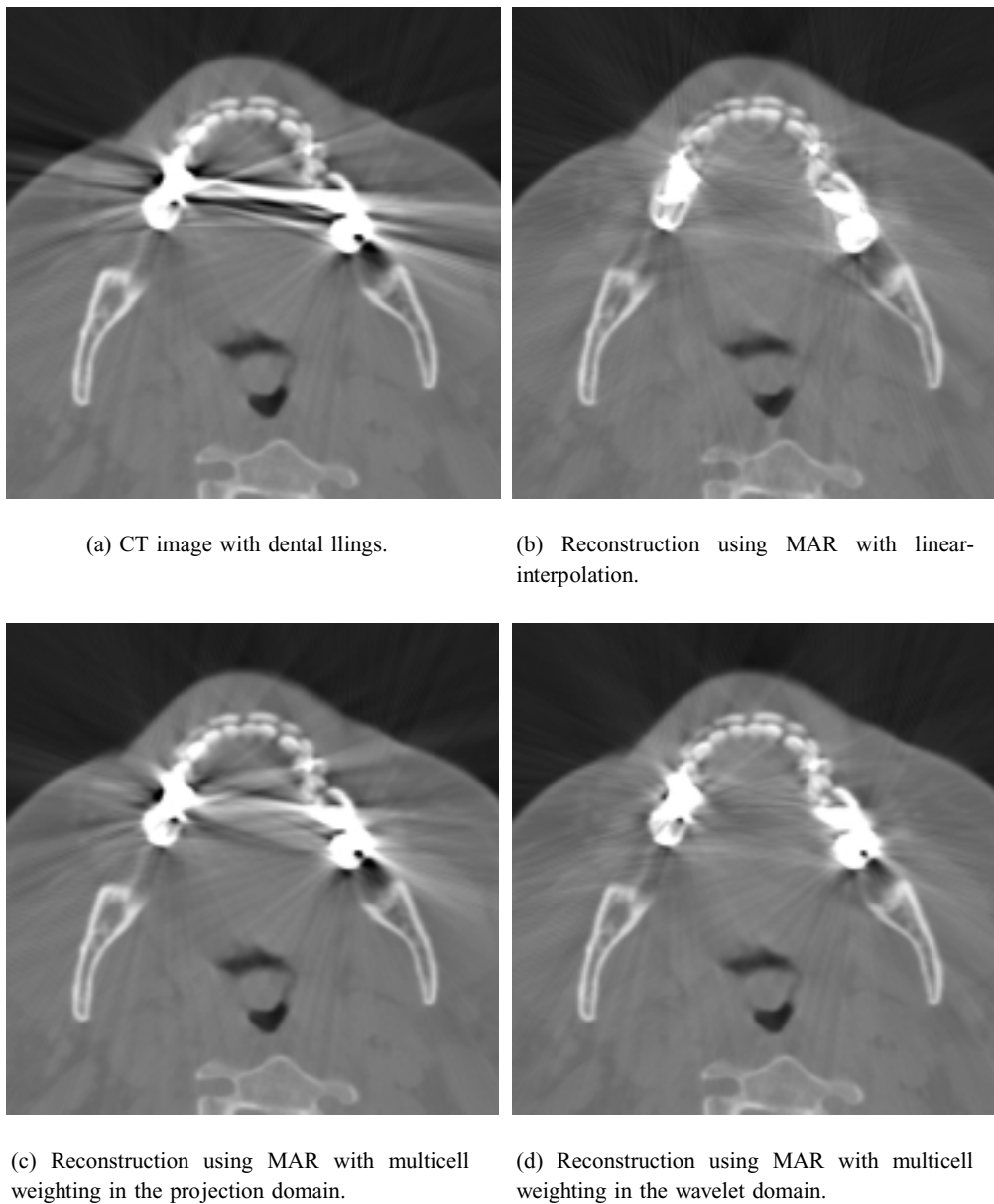
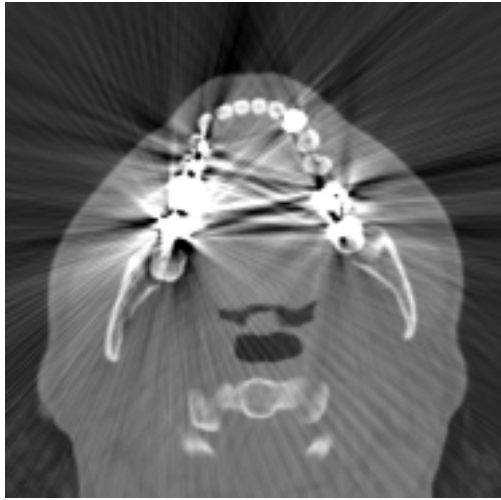
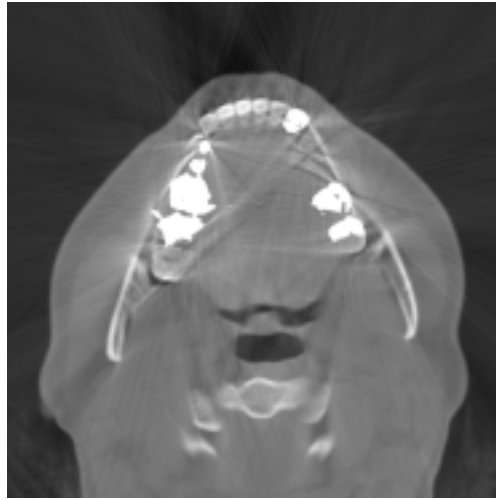


Fig. 4. Dental case study I.

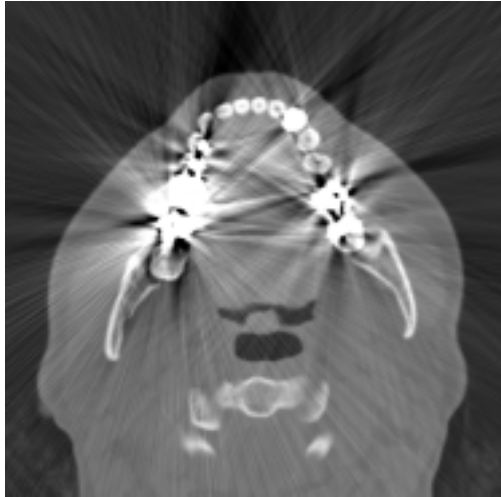
Comparing subfigures (c) and (d) in Figs 3–5, it is observed that WMI did not render some portions of bony structure as well as their counterparts in the project domain, because the badly damaged wavelet components in coarser scale-levels were replaced by the corresponding components from linear-interpolated data. It is also recognized that all methods were not effective between the two copper cylinders in the second phantom experiment. As we remarked in [1], a physical reason for this defect is that the two cylinders are too close to each other with respect to the scan resolution (768 channels per view). As a result, there was not much information without the contamination of these metallic objects collected for reconstruction from that region.



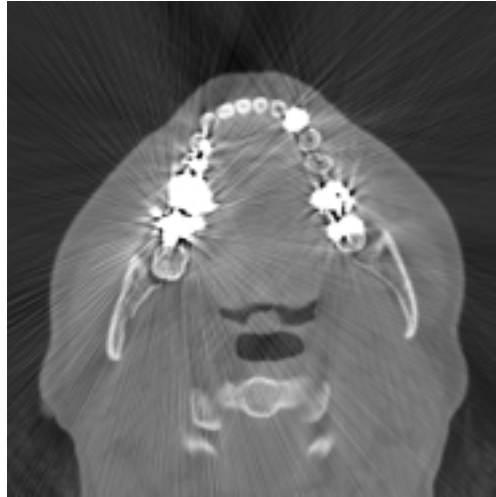
(a) CT image with dental fillings.



(b) Reconstruction using MAR with linear-interpolation.



(c) Reconstruction using MAR with multicell weighting in the projection domain.



(d) Reconstruction using MAR with multicell weighting in the wavelet domain.

Fig. 5. Dental case study II.

4. Discussion and conclusion

WMI is a recent advance for MAR with linear-interpolation. It makes use of a scale-level dependent linear interpolation of wavelet coefficients of scan data and linear-interpolated data to compensate for data corruption and reveal diagnostic information from the data contaminated by multiple highly attenuating implants in the FOV. Our experimental results demonstrated that WMI with the proposed multicell weighting can produce excellent images by optimally balancing metal artifact reductions and feature details surrounding metallic objects.

The current implementation of WMI relies on weighting schema designed from the qualitative analysis of metal artifacts. Parameters in our algorithms are manually selected. Although any choice of the parameters in their reasonable ranges would improve the image quality to a certain degree, the optimal parameter settings is a focus of our further work.

Our approach is to emulate (statistical) iterative methods for MAR [13–19]. By reformulating the penalized maximum likelihood method in terms of the weights $\lambda_{j,k}$ used in the wavelet interpolation Eq. (3), we may obtain a target function for optimization with our weighting strategies as Gibbs priors. To minimize the computational overhead, we only estimate a sample of the weights $\lambda_{j,k}$ for each scale-level j , using the methods of expectation-maximization (EM) [20] or maximum *a posteriori* (MAP) [21], and smoothly extend them to a complete set of weights. We believe that this approach will enable us to automate the parameter estimation procedure, and lead to a nearly optimal selection of the weights $\lambda_{j,k}$ for wavelet interpolation.

In conclusion, we have developed a practical and efficient wavelet MAR method. Utilizing wavelet space–frequency localization, this method fully uses the information in CT scan data, effectively corrects the high attenuation effects due to multiple metallic objects in the FOV. Heavy metal artifacts can be mostly eliminated from the reconstructed images while morphological details are faithfully retained, especially in the vicinity of multiple metallic objects. The computational overhead is negligible. Therefore, our results have demonstrated that this wavelet method is promising for MAR and has potential to be used in clinical practice.

References

- [1] S. Zhao, D.D. Robertson, G. Wang, B. Whiting and K.T. Bae, X-ray CT metal artifact reduction using wavelets: An application for imaging total hip prostheses, *IEEE Trans. Med. Imag.* **12**(12) (2000), 1238–1247.
- [2] N. Strumas, O. Antonyshyn, M.J. Yaffe, G. Mawdsley and P. Cooper, Computed tomography artefacts: An experimental investigation of causative factors, *Can. J. Plast. Surg.* **6**(1) (1998), 23–29.
- [3] B. De Man, *Iterative Reconstruction for Reduction of Metal Artifacts in Computed Tomography*, Ph.D. thesis, Katholieke Universiteit Leuven, 2001.
- [4] R.M. Lewitt and R.H.T. Bates, Image reconstruction from projections: III: Projection completion methods, *Optik* **50** (1978), 189–204.
- [5] T. Hinderling, P. Rueggsegger, M. Anliker and C. Dietschi, Computed tomography reconstruction from hollow projections: An application to in vivo evaluation of artificial hip joints, *J. Comput. Assist. Tomogr.* **3** (1979), 52–57.
- [6] W.A. Kalender, R. Hebel and J. Ebersberger, Reduction of CT artifacts caused by metallic implants, *Radiology* **164** (1987), 576–577.
- [7] C.R. Crawford, J.G. Colsher, N.J. Pelc and A.H.R. Lonn, High speed reprojection and its applications, *SPIE Medical Imaging II* **914** (1988), 311–318.
- [8] E. Klotz, W.A. Kalender, R. Sokiranski and D. Felsenberg, Algorithms for reduction of CT artifacts caused by metallic implants, *SPIE Medical Imaging IV: PACS System Design and Evaluation* **1234** (1990), 642–650.
- [9] A. Rosenfeld and A.C. Kak, *Digital Picture Processing*, (Vol. 1), (2nd ed.), Academic Press, New York, 1982.
- [10] F. Natterer, *The Mathematics of Computerized Tomography*, John Wiley and Sons, New York, 1986.
- [11] A. Cohen, I. Daubechies and J. Feauveau, Biorthogonal bases of compactly supported wavelets, *Comm. Pure Appl. Math.* **45** (1992), 485–560.
- [12] I. Daubechies, *Ten Lectures on Wavelets*, CBMS-NSF Series in Applied Mathematics, SIAM, Philadelphia, 1992.
- [13] R.W. Gerchberg, Super-resolution through error energy reduction, *Optica Acta* **21** (1974), 709–720.
- [14] A. Papoulis, A new algorithm in spectral analysis and band-limited extrapolation, *IEEE Trans. on Circuits and Systems* **22** (1975), 735–742.
- [15] M. Nassi, W.R. Brody, B.P. Medoff and A. Macovski, Iterative reconstruction-reprojection: an algorithm for limited data cardiac computed tomography, *IEEE Trans. Biomed. Eng.* **29** (1982), 333–341.
- [16] B.P. Medoff, W.R. Brody, M. Nassi and A. Macovski, Iterative convolution backprojection algorithms for image reconstruction from limited data, *J. Opt. Soc. Am.* **73** (1983), 1493–1500.
- [17] M.I. Sezan and H. Stark, Tomographic image reconstruction from incomplete view data by convex projections and direct fourier inversion, *IEEE Trans. Med. Imag.* **3** (1984), 91–98.

- [18] G. Wang, D.L. Snyder, J.A. O'Sullivan and M.W. Vannier, Iterative deblurring for CT metal artifact reduction, *IEEE Trans. Med. Imag.* **15** (1996), 657–664.
- [19] D.D. Robertson, J. Yuan, G. Wang and M.W. Vannier, Total hip prosthesis metal-artifact suppression using iterative deblurring reconstruction, *J. Comput. Assist. Tomogr.* **21** (1997), 293–298.
- [20] L. Shepp and Y. Vardi, Maximum likelihood reconstruction for emission tomography, *IEEE Trans. Med. Imag.* **1** (1982), 113–122.
- [21] S. Geman and D. Geman, Stochastic relaxation, gibbs distributions and the bayesian restoration of images, *IEEE Trans. Patt. Anal. Mach. Intell.* **6** (1984), 721–741.